Available online at www.sciencedirect.com

ScienceDirect

IFAC PapersOnLine 58-28 (2024) 210–215

Experimental Model Identification of the Longitudinal Dynamics of an Electric Unicycle with a Human Rider[⋆]

Levente Mihályi[*], **Xunbi A. Ji**[**], **Gábor Orosz**[**,***],
and **Dénes Takács**[*,****]

[*] *Department of Applied Mechanics, Faculty of Mechanical Engineering, Budapest University of Technology and Economics, Műegyetem rkp. 3, Budapest, H–1111, Hungary (e-mail: mihalyi@mm.bme.hu, takacs@mm.bme.hu).*
[**] *Department of Mechanical Engineering, University of Michigan, Ann Arbor, MI 48109, USA (e-mail: xunbij@umich.edu, orosz@umich.edu).*
[***] *Department of Civil and Environmental Engineering, University of Michigan, Ann Arbor, MI 48109, USA*
[****] *HUN-REN–BME Dynamics of Machines Research Group, Budapest, Hungary*

Abstract: A model for the longitudinal and pitch dynamics of an electric unicycle (EUC) ridden by a human is derived while considering the independent pitch movements of the EUC body and that of the rider. Experimental data is collected for multiple maneuvers through a high-precision motion capture system and the processed data is used for parameter identification. It is demonstrated that the longitudinal and pitch dynamics are well captured by the model even for maneuvers which involve lateral motion.

Keywords: Electric unicycle, motion capture, system modeling, parameter identification, human and vehicle interaction

1. INTRODUCTION

In modern urban transportation, micromobility vehicles offer a compact, sustainable solution for short-distance commutes and delivery tasks of food or lighter goods. With their high maneuverability, electric unicycles (EUCs) provide efficient transportation through congested streets, bypassing traffic jams and thereby reducing travel time. Also, their portability allows for seamless integration with other types of transportation.

Electric unicycles require special design and development due to the complexity of their dynamics. The unstable nature of their motion can be attributed to the large ratio of the mass of the rider to the mass of the vehicle itself. EUCs give the riders high level of agility, however, they also make motion predictions difficult for the developers. The rider acts as an inverted pendulum on the moving EUC, and the dynamics of the system are mostly determined by the leaning and turning of the human body. While human-powered unicycles were investigated in (Sheng and Yamafuji, 1995; Niełaczny et al., 2019), the dynamics of human-ridden electric unicycles are mostly unexplored. Seated EUCs can be modeled in a simpler way since the human body and the frame of the device can be considered as a single body (Li et al., 2012; Chen et al., 2016), and sometimes standing EUCs are assumed to behave similarly (Tsai et al., 2015).

In this study, a more sophisticated model representing the longitudinal dynamics is introduced, in which the human can lean forward and backward independent of the EUC body. This extension may shed light on the interaction between the rider and the vehicle. By separating the longitudinal and lateral dynamics, the complicated spatial motion is simplified to planar cases. Another major contribution of this work is the experimental investigation of various maneuvers of a human-ridden EUC. Detailed experimental tests provide relevant information about the motion control performed by human riders. Using our simplified model and the collected data, the driving torque is estimated based on the measured kinematic variables of the longitudinal motion, and the system parameters are identified. This research leads to better understanding of how riders control their electric unicycles. The results may be helpful for developing rider assist features which can improve the safety of these micromobility vehicles while being seamlessly integrated into the control units of electric unicycles.

The rest of the paper is organized as follows. We first present our experimental setup and data extraction in Section 2. Then we present the mechanical model for the longitudinal and pitch motion of the EUC with the rider, and derive the corresponding mathematical model in

---

[⋆] This research was supported by the National Research, Development and Innovation Office of Hungary under grant no. NKFI-146201. DT is also supported by the János Bolyai Research Scholarship of the Hungarian Academy of Sciences. GO acknowledges the support of the Hungarian Academy of Sciences within the Distinguished Guest Fellowship Programme and the support of the Fulbright Foundation.

Peer review under responsibility of International Federation of Automatic Control.
10.1016/j.ifacol.2024.12.036

Section 3. In Section 4, we identify the model parameters using the experimental data. We summarize the results and discuss future research directions in Section 5.

2. EXPERIMENTAL INVESTIGATION OF EUC DYNAMICS

To investigate the dynamics of the human-ridden EUC we generated an experimental dataset using a high-precision motion capture system. This dataset consists of 34 recordings, covering 8 maneuvers, accomplished by two riders of different riding levels; see Table 1. The maneuvers were selected such that both longitudinal and lateral balancing were required while riders were facing different levels of difficulties in executing the maneuvers. In this study, we focus on the constant speed, acceleration, deceleration, and figure-eight maneuvers.

Table 1. Different maneuvers and recordings

Maneuver	number of recordings
Constant speed	7
Acceleration	3
Deceleration	2
Circling	6
U-turn	8
Slalom	5
Figure-eight	2
Riding on one leg	1
Total	34

To collect motion data, an *OptiTrack* motion capture system was utilized. The experimentally observed volume of approximately $6 \times 4 \times 2$ meters was covered by 12 cameras. The accuracy of detection is ± 0.20 mm in position and $\pm 0.5^\circ$ in rotational angles. This sensor apparatus provides position and orientation data at a frequency of 120 Hz for all rigid bodies listed in Table 2. The body segments were selected with the consideration that they play significant roles in the dynamics of the human while riding the unicycle. Note that for paired body segments, the last letters of the abbreviations refer to right (R) and left (L); see also Fig. 1.

Table 2. Defined rigid bodies and pivot points

Abbreviation	Body segment	Pivot point
H	Head	Top of the helmet
CHR, CHL	Chest	Shoulder
UAR, UAL	Upper arm	Elbow
LAR, LAL	Lower arm	Wrist
HR, HL	Hip	Hip
TR, TL	Thigh	Knee
LR, LL	Leg	Ankle
E	EUC	Top of the EUC

Each rigid body was defined using at least four markers in the motion tracking system, including a pivot point for each body. These pivot points were traced in time, and the spatial orientations of the rigid bodies were also detected. Namely, the positions are given in the ground-fixed coordinate system (X, Y, Z), while the rotational data are described by Euler angles for which we use the sequence of yaw-tilt-pitch. In the case of the EUC, these angles are shown in Fig. 2 by ψ, ϑ and γ.

Based on the captured data related to the human body segments, we reconstructed our skeleton model and calculated

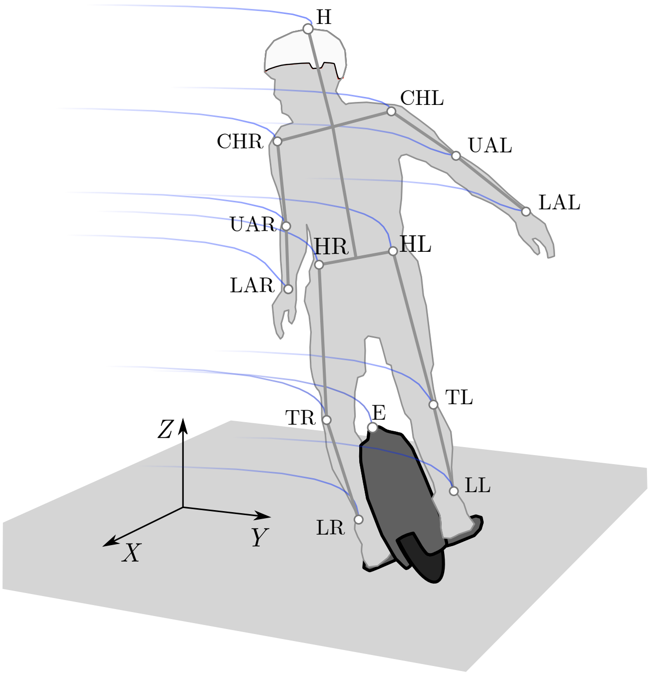

Fig. 1. Skeleton model of the human standing on the EUC. Blue curves illustrate trajectories of pivot points related to different body segments.

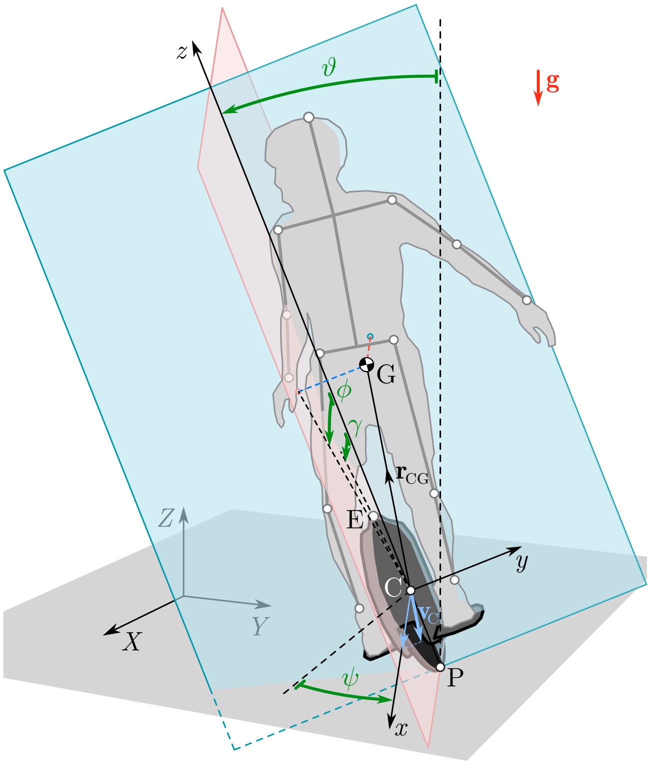

Fig. 2. The longitudinal (red) and frontal (blue) planes of the EUC body rotated by the yaw angle ψ and tilt angle ϑ. The pitch angles of the EUC body and rider are denoted by γ and ϕ, respectively.

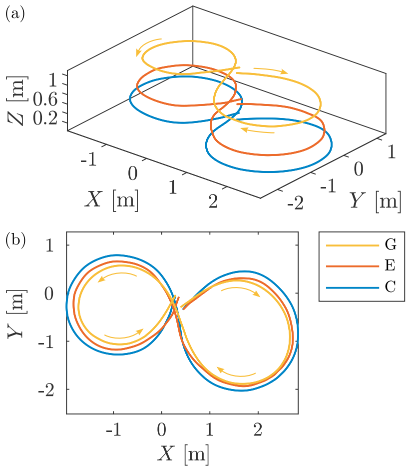

Fig. 3. Trajectories of a figure-eight maneuver in the ground-fixed frame (X, Y, Z) showing the motion of the wheel's center point C, the EUC's pivot point E, and the rider's center of gravity G.

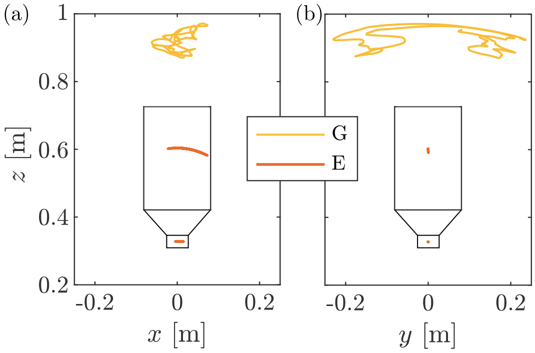

Fig. 4. Trajectories of a figure-eight maneuver in the moving frame (x, y, z) showing the motion of the EUC's pivot point E and the rider's center of gravity G. The projections of the trajectories are shown (a) in the longitudinal plane (x, z) and (b) in the frontal plane (y, z).

the rider's center of gravity G. The masses of the body segments were estimated based on (Ramachandran et al., 2016) and the rider's known overall mass. The position of the EUC's wheel center point C was determined by using the measured position of the pivot point E, the measured yaw, tilt and pitch angles of the EUC body, and the known constant distance between C and E. Hence, the vector $\mathbf{R}_{\mathrm{CG}} = [X_{\mathrm{CG}}, Y_{\mathrm{CG}}, Z_{\mathrm{CG}}]^{\top}$ which gives the position of the rider's center of gravity G relative to the wheel center C can be calculated in the ground-fixed coordinate system (X, Y, Z).

For instance, the position data of a figure-eight maneuver are presented in Fig. 3, where the trajectories of the EUC's pivot point E, the wheel's center point C and the rider's center of gravity G are plotted in the ground-fixed coordinate system (X, Y, Z). Note that the time signals were smoothed using the Savitzky–Golay method, by which the derivatives of the smoothed signal were calculated analytically for the parameter identification carried out in Section 4.

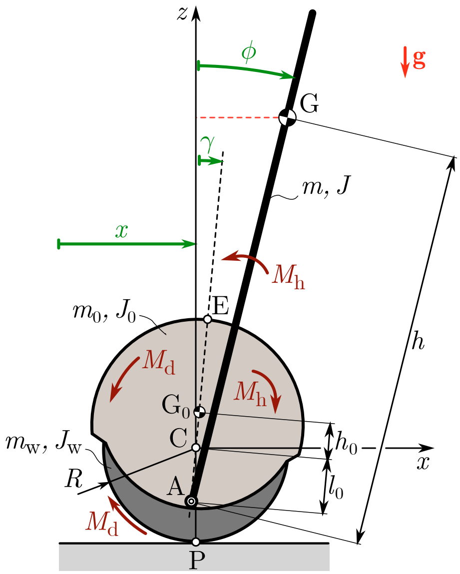

Fig. 5. Mechanical model representing the longitudinal and pitch dynamics of the EUC–rider system. Parameters are collected and explained in Table 3.

The position vector $\mathbf{r}_{\mathrm{CG}} = [x_{\mathrm{CG}}, y_{\mathrm{CG}}, z_{\mathrm{CG}}]^{\top}$ of the rider's center of gravity G can also be determined in the moving frame (x, y, z); see Fig. 2. This frame is fixed to the wheel center point C, and its yaw and tilt angles correspond to the yaw ψ and tilt ϑ angles of the EUC. The transformation between the ground-fixed frame (X, Y, Z) and the moving frame (x, y, z) is carried out by

$$\mathbf{r}_{\mathrm{CG}} = \mathbf{T}_{\vartheta}^{\top} \mathbf{T}_{\psi}^{\top} \mathbf{R}_{\mathrm{CG}} \,, \tag{1}$$

where the transformation matrices read

$$\mathbf{T}_{\psi} = \begin{bmatrix} \cos\psi & -\sin\psi & 0 \\ \sin\psi & \cos\psi & 0 \\ 0 & 0 & 1 \end{bmatrix}, \quad \mathbf{T}_{\vartheta} = \begin{bmatrix} 1 & 0 & 0 \\ 0 & \cos\vartheta & -\sin\vartheta \\ 0 & \sin\vartheta & \cos\vartheta \end{bmatrix}. \tag{2}$$

The longitudinal plane (x, z) and the frontal plane (y, z) of the EUC body are defined as shown in red and blue in Fig. 2, respectively. In Fig. 4, the relative motion of the EUC's pivot point E and the rider's center of gravity G is shown in these planes for the figure-eight maneuver. Later on, we will use the location of G projected into the longitudinal plane to approximate the rider's pitch angle as

$$\phi = \arctan \frac{x_{\mathrm{CG}}}{z_{\mathrm{CG}}} \,. \tag{3}$$

This way, we can use the experimental data to identify model parameters according to the model of Section 3.

The longitudinal velocity and acceleration of the wheel center point C are calculated by transforming the velocity vector $\mathbf{v}_{\mathrm{C}} = \dot{\mathbf{R}}_{\mathrm{C}}$ and acceleration vector $\mathbf{a}_{\mathrm{C}} = \ddot{\mathbf{R}}_{\mathrm{C}}$ into the moving frame (x, y, z) and taking their longitudinal components $v_{\mathrm{C}x}$ and $a_{\mathrm{C}x}$, respectively; see Fig. 2. These correspond to the speed $\dot{x}$ and acceleration $\ddot{x}$ in the model presented in Section 3.

3. MODELING THE LONGITUDINAL AND PITCH DYNAMICS

In this section, to simplify the analysis, we assume that the effect of the lateral dynamics is small and we focus

Table 3. Model parameters

Parameters	Value
Wheel radius R	0.2 m
Human body's mass m	65 kg
EUC total mass $(m_0 + m_\mathrm{w})$	16 kg
EUC body's mass m_0	13 kg
EUC wheel's mass m_w	3 kg
Human body's mass moment of inertia	16.6 kg·m^2
EUC wheel's mass moment of inertia	0.12 kg·m^2
EUC body's mass moment of inertia	0.5 kg·m^2
Distance (C–G$_0$) h_0	0.075 m
Distance (A–C) l_0	0.05 m
Distance (A–G) h	to be identified

on the longitudinal dynamics only. We derive a detailed mechanical model to describe the longitudinal and pitch dynamics of the EUC–rider system.

We describe the longitudinal and pitch dynamics by the three-degree-of-freedom (3 DoF) mechanical model shown in Fig. 5, where the pitch motion of the EUC and that of the rider are separated. The pitch angles are denoted by γ and ϕ for the EUC body and for the human body, respectively. These serve as (positional) generalized coordinates for our system. The third (cyclic) generalized coordinate x is the longitudinal position of the wheel's center point C, where the EUC body and wheel are coupled via a joint. Point G represents the rider's center of gravity, and point G$_0$ is the EUC's center of gravity. The hinge point A models the connection between the EUC and the rider. Since the rider's feet are fixed to the pedals of the EUC during the rides, the hinge point corresponds to the rider's ankle. Point P is the wheel-ground contact point, whose velocity is zero in case of pure rolling, i.e., $\mathbf{v}_\mathrm{P} = \mathbf{0}$.

The other parameters of the model are the distance h measured between the center of gravity G and the hinge point A; the distance h_0 between the EUC's center of gravity G$_0$ and the wheel's center C; and the distance l_0 is measured from the hinge point A to the wheel's center C. Masses and mass moments of inertia are denoted by m and J, distinguished by the subscripts as follows: the human body (without subscript), the EUC body (subscript 0), and the wheel (subscript w). The radius of the wheel is denoted by R. The parameters with their numerical values are collected in Table 3.

There are two actuating efforts in the model: the electric motor's driving torque M_d and the human control torque M_h. Note that both torques are internal, i.e., the driving torque acts between the wheel and the EUC body, while the human control torque acts between the EUC body and the human body. Accordingly, the torques and counteracting torques are shown in Fig. 5. Note that the driving torque is commanded by the EUC's inner controller, and the embedded control law is likely based on the pitch angle γ and pitch rate $\dot{\gamma}$ but unknown to us.

3.1 Equations of motion

The governing equations are derived using the Lagrange equations of the second kind

$$\frac{\mathrm{d}}{\mathrm{d}t}\frac{\partial T}{\partial \dot{\mathbf{q}}} - \frac{\partial T}{\partial \mathbf{q}} = \mathbf{Q}\,, \tag{4}$$

where the vector $\mathbf{q} = [x\ \gamma\ \phi]^\top$ contains the generalized coordinates. The expression of the kinetic energy T and the identification of the generalized force vector $\mathbf{Q}$ via the virtual power is detailed in Appendix A. The equations of motion can be arranged in the form

$$\mathbf{M}(\mathbf{q})\,\ddot{\mathbf{q}} + \mathbf{h}(\dot{\mathbf{q}}, \mathbf{q}) = \mathbf{Q}(\mathbf{q}). \tag{5}$$

The elements of the mass matrix $\mathbf{M} = [m_{ij}]$ are

$$\begin{aligned} m_{11} &= m + m_0 + m_\mathrm{w} + J_\mathrm{w}/R^2\,, \\ m_{12} &= m_{21} = -(ml_0 - m_0 h_0)\cos\gamma\,, \\ m_{13} &= m_{31} = mh\cos\phi\,, \\ m_{22} &= J_0 + m_0 h_0^2 + m l_0^2\,, \\ m_{23} &= m_{32} = -mhl_0\cos\left(\phi - \gamma\right), \\ m_{33} &= J + mh^2. \end{aligned} \tag{6}$$

The vector $\mathbf{h}$ contains the nonlinear terms not related to the generalized accelerations:

$$\mathbf{h} = \begin{bmatrix} -mh\dot{\phi}^2\sin\phi + (ml_0 - m_0h_0)\dot{\gamma}^2\sin\gamma \\ mhl_0\dot{\phi}^2\sin\left(\phi - \gamma\right) \\ -mhl_0\dot{\gamma}^2\sin\left(\phi - \gamma\right) \end{bmatrix}. \tag{7}$$

The generalized force vector containing the active forces is

$$\mathbf{Q} = \begin{bmatrix} M_\mathrm{d}/R \\ M_\mathrm{h} - M_\mathrm{d} + (m_0h_0 - ml_0)g\sin\gamma \\ mgh\sin\phi - M_\mathrm{h} \end{bmatrix}. \tag{8}$$

One can express the driving torque M_d from (5), if all the states x, γ and ϕ are measured and their first and second derivatives are numerically calculated. Since there are three equations in (5) and two unknowns (M_d, M_h), one can determine two independent expressions for the driving torque M_d. For example, from the first row of (5) the driving torque reads as

$$M_\mathrm{d} = M_{\mathrm{d},1}(\gamma, \phi, \dot{\gamma}, \dot{\phi}, \ddot{\gamma}, \ddot{\phi}, \ddot{x}) \tag{9}$$

On the other hand, using all three rows of (5) and eliminating $\ddot{x}$, the driving torque can also be calculated by a different expression:

$$M_\mathrm{d} = M_{\mathrm{d},2}(\gamma, \phi, \dot{\gamma}, \dot{\phi}, \ddot{\gamma}, \ddot{\phi}). \tag{10}$$

If the actual driving torque M_d was measured, one can identify all model parameters (see Table 3) by minimizing the difference between the measured M_d and the model-based expression (9) or (10). However, the driving torque was not measurable in our experiments. Therefore, we use nominal parameters based on prior knowledge and only identify h, the distance between the riders's center of gravity G and the hinge point A, through minimizing the difference between $M_{\mathrm{d},1}$ and $M_{\mathrm{d},2}$.

3.2 Reduced model

The model constructed above is also compared to a simpler one developed by Molnár et al. (2023). The reduced model can be obtained by neglecting the mass moment of inertia of the EUC body and coinciding the wheel's center, the EUC body's center and the hinge points (A ≡ C ≡ G$_0$), i.e., considering $J_0 = 0$, $h_0 = 0$ and $l_0 = 0$. With these assumptions the model (5)–(8) simplifies to

$$\overline{\mathbf{M}} = \begin{bmatrix} m + m_0 + m_\mathrm{w} + J_\mathrm{w}/R^2 & 0 & mh\cos\phi \\ 0 & 0 & 0 \\ mh\cos\phi & 0 & J + mh^2 \end{bmatrix}, \tag{11}$$

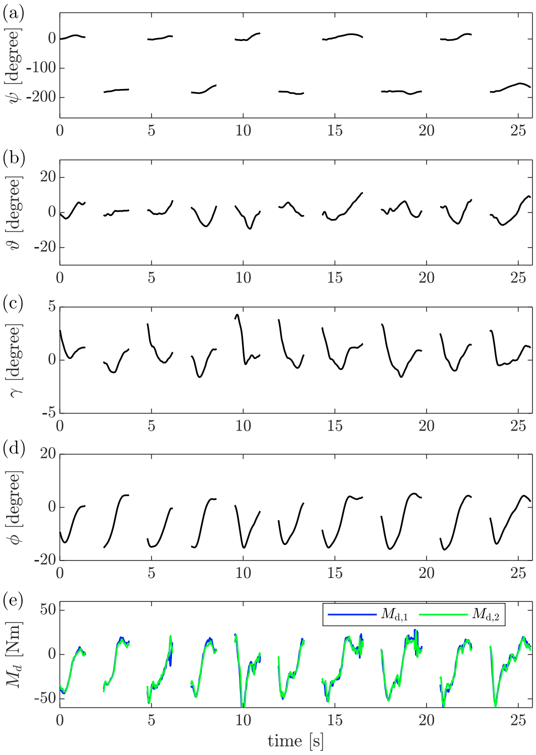

Fig. 6. Processed data of deceleration maneuvers (10 runs). (a) Yaw angle ψ of the EUC. (b) Tilt angle ϑ of the EUC. (c) Pitch angle γ of the EUC. (d) Pitch angle ϕ of the human rider. (e) Driving torque of the EUC given by the 3 DoF model with the optimized height $h = 0.61$ m. The root-mean-squared error (RMSE) between $M_{d,1}$ and $M_{d,2}$ is 4.7599 Nm.

$$\overline{\mathbf{h}} = \begin{bmatrix} -mh\dot{\phi}^2 \sin\phi \\ 0 \\ 0 \end{bmatrix}, \; \overline{\mathbf{Q}} = \begin{bmatrix} M_\mathrm{d}/R \\ M_\mathrm{h} - M_\mathrm{d} \\ mgh\sin\phi - M_\mathrm{h} \end{bmatrix}. \tag{12}$$

Note that the second equation gives $M_\mathrm{d} = M_\mathrm{h}$, that is, the 3 DoF model is simplified to a 2 DoF model. Moreover, the expressions (9)–(10) of the driving torque provide

$$\begin{aligned} \overline{M}_{\mathrm{d},1} =& -mhR\sin\phi\dot{\phi}^2 + m_\mathrm{eq}R\ddot{x} + mhR\cos\phi\ddot{\phi}\,, \\ \overline{M}_{\mathrm{d},2} =& \frac{m_\mathrm{eq}mghR\sin\phi}{mh\cos\phi + m_\mathrm{eq}R} - \frac{m^2h^2R\sin\phi\cos\phi}{mh\cos\phi + m_\mathrm{eq}R}\dot{\phi}^2 \\ &+ \frac{m^2h^2R\cos^2\phi - m_\mathrm{eq}R(J + mh^2)}{mh\cos\phi + m_\mathrm{eq}R}\ddot{\phi}\,, \end{aligned} \tag{13}$$

where $m_\mathrm{eq} = m + m_0 + m_\mathrm{w} + J_\mathrm{w}/R^2$.

4. PARAMETER IDENTIFICATION

In this section, we identify the height h of the human center of gravity from the experimental data presented in Section 2 while using the model (5)–(8). Although the value of h may change with the rider's motion during the maneuver, we still consider it as a constant to maintain simplicity. The models can be improved by considering the time-varying parameters in the future studies. We also compare the results to those given by the simplified model (5),(11)–(12).

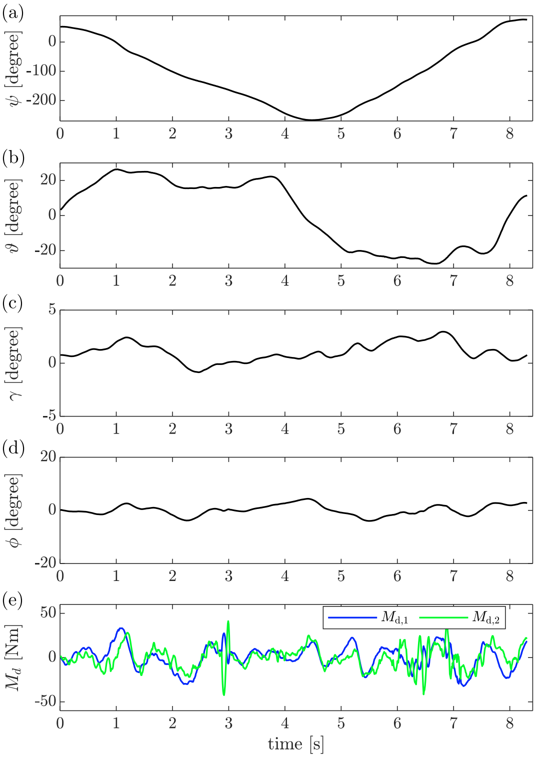

Fig. 7. Processed data for a figure-eight maneuver (1 run). (a) Yaw angle ψ of the EUC. (b) Tilt angle ϑ of the EUC. (c) Pitch angle γ of the EUC. (d) Pitch angle ϕ of the human rider. (e) Driving torque of the EUC given by the 3 DoF model with the optimized height $h = 0.28$ m. The RMSE between $M_{d,1}$ and $M_{d,2}$ is 13.5626 Nm.

We present the processed data of deceleration and figure-eight maneuvers in Fig. 6 and Fig. 7, respectively. The yaw angle ψ and tilt angle ϑ of the EUC are plotted in panels (a) and (b), respectively. These show dynamics that are not captured by the models of Section 3. Note that the yaw angle alternates between values around 0 and $-180°$ because the direction of the straight running motion changes thanks to U-turns performed outside the area of recording.

In Fig. 6(c) and Fig. 7(c), one can observe that the pitch angle γ of the EUC body remains small for both cases. In the deceleration case, observe that the pitch angle ϕ of the human is negative as the rider leans back to reduce the speed; see Fig. 6(d). Correspondingly, the pitch angle γ of the EUC also decreases in Fig. 6(c).

By minimizing the difference between $M_{\mathrm{d},1}$ and $M_{\mathrm{d},2}$ using (9)–(10), we obtain the optimal h for the 3 DoF model. The driving torque given by (9) and (10) are plotted in Fig. 6(e) and Fig. 7(e) for the optimal h in each maneuver. The driving torques obtained from the different expressions match well in the case of the deceleration maneuver. For the figure-eight maneuver, $M_{\mathrm{d},1}$ and $M_{\mathrm{d},2}$ are also consistent, although the difference is larger due to the ignored lateral and tilt dynamics. These results show that the first-principle-based in-plane model of our study captures the longitudinal and pitch dynamics well when the lateral motion and tilt angle are small, and can be used to calculate the driving torque from experimental data.

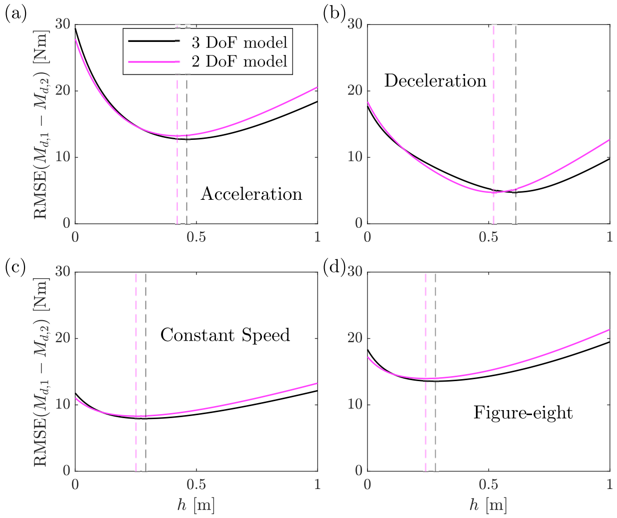

Fig. 8. Comparison of the error of the two models on four different recordings

The root-mean-squared error (RMSE) between $M_{\mathrm{d},1}$ and $M_{\mathrm{d},2}$ is plotted as a function of h in Fig. 8 for four different maneuvers: constant speed, acceleration, deceleration, and figure-eight. The driving torques are calculated for the 3 DoF model using (9)–(10) and for the 2 DoF model using (13). Although the difference between these two models is not significant due to the small pitch angle of the EUC body, the 3 DoF model has smaller errors at the minima and identifies a larger (more realistic) height h.

The identified value of h varies for the four different recordings. On the one hand, the vertical position of the rider's center of gravity may depend on the maneuver type. On the other hand, our model may describe the real system with different precision in case of different maneuvers. Among the four recordings, the deceleration dataset provides the smallest error at the optimal h, while the figure-eight dataset gives the largest. This shows that the developed model captures the longitudinal and pitch dynamics well for the deceleration maneuver (which has negligible yaw, lateral and tilt motion), but the yaw, lateral, and tilt dynamics play a more relevant role in the figure-eight case (where the tilt angle and yaw rate are significantly larger).

For the constant-speed and figure-eight maneuvers the error curves in Fig. 8(c)–(d) are relatively flat (a large range of h gives similar torque values). This indicates that those two data sets are not sensitive to the height h, making it difficult to infer this parameter. This is because the constant-speed maneuver is operated around the equilibrium of the system, while the figure-eight data includes significant lateral dynamics that is not captured by the models developed in this paper.

5. CONCLUSION

In this paper, we analyzed the motion of an electric unicycle with a human rider using a series of experiments. We constructed a mechanical model for the longitudinal and pitch motion and used this model to obtain the EUC driving torque from high-precision motion capture data. Then, we identified the height of the rider's center of gravity. It was shown that our model yields smaller errors and more realistic parameters compared to a simplified model of the literature. We also showed that the longitudinal model performs well for straight running motions, and it can also be used for more complex maneuvers. With the developed models and the driving torque calculations, the EUC's torque controller may be identified in the future. We plan to carry out more extensive experiments and study human motion control with the longitudinal models. Comparing the current first-principle-based model to data-driven models is also a possible topic of future research.

REFERENCES

Chen, P.C., Pan, S.M., Chuang, H.S., and Chiang, C.H. (2016). Dynamics analysis and robust control for electric unicycles under constrained control force. *Arabian Journal for Science and Engineering*, 41(11), 4487–4507.

Li, Y.Y., Tsai, C.C., and Lin, C.M. (2012). Intelligent adaptive steering control for electric unicycles. In *IEEE International Conference on Systems, Man, and Cybernetics (SMC)*, 2457–2462.

Molnár, T., Kiss, A., Ames, A., and Orosz, G. (2023). Safety-critical control with input delay in dynamic environment. *IEEE Transactions on Control Systems Technology*, 31(4), 1507–1520.

Niełaczny, M., Wiesław, B., and Kapitaniak, T. (2019). *Dynamics of the Unicycle Modelling and Experimental Verification*. Springer.

Ramachandran, H., Vasudevan, D., Brahma, A., and Pugazhenthi, S. (2016). Estimation of mass moment of inertia of human body, when bending forward, for the design of a self-transfer robotic facility. *Journal of Engineering Science and Technology*, 11, 166–176.

Sheng, Z. and Yamafuji, K. (1995). Study on the stability and motion control of a unicycle: Part I: Dynamics of a human riding a unicycle and its modeling by link mechanisms. *JSME International Journal, Series C*, 38(2), 249–259.

Tsai, C.C., Li, Y.Y., and Tai, F.C. (2015). Nonlinear self-balancing and speed control using WFCMAC for seatless electric unicycles. In *10th Asian Control Conference (ASCC)*.

Appendix A. KINETIC ENERGY AND VIRTUAL POWER

The kinetic energy of the mechanical system in Fig. 5 can be calculated as

$$\begin{aligned} T =& \frac{1}{2}\left(m + m_0 + m_\mathrm{w} + \frac{J_\mathrm{w}}{R^2}\right)\dot{x}^2 \\ &+\frac{1}{2}\left(J_0 + ml_0^2 + m_0h_0^2\right)\dot{\gamma}^2 + \frac{1}{2}\left(J + mh^2\right)\dot{\phi}^2 \\ &-(ml_0 - m_0h_0)\dot{x}\dot{\gamma}\cos\gamma + mh\dot{x}\dot{\phi}\cos\phi \\ &-mhl_0\dot{\gamma}\dot{\phi}\cos(\phi-\gamma)\,. \end{aligned} \tag{A.1}$$

The virtual power of the active forces can be expressed as

$$\begin{aligned} \delta P =& \frac{M_\mathrm{d}}{R}\delta\dot{x} + (mgh\sin\phi - M_\mathrm{h})\delta\dot{\phi} \\ &+ \left(M_\mathrm{h} - M_\mathrm{d} + (m_0h_0 - ml_0)g\sin\gamma\right)\delta\dot{\gamma}\,. \end{aligned} \tag{A.2}$$

Then the generalized force vector can be identified from the coefficients of the virtual generalized velocities, i.e., $\delta P = \mathbf{Q}\cdot\delta\dot{\mathbf{q}}$ where $\cdot$ refers to the dot product.